REPORT DOCUMENTATION PAGE

Form Approved
OMB NO. 0704-0188

1. AGENCY USE ONLY (Leave Blank)	2. REPORT DATE 6/30/03	3. REPORT TYPE AND DATES COVERED Final Progress Report, 01 Jun 99 - 31 AUG 02

4. TITLE AND SUBTITLE
Biomolecular Recognition of Semiconductors and Magnetic Materials to Pattern Quantum Confined and Magnetoelectronic Structures

5. FUNDING NUMBERS
DAAD-19-99-1-0155

6. AUTHOR(S)
Angela M. Belcher

7. PERFORMING ORGANIZATION NAME(S) AND ADDRESS(ES)
University of Texas - Austin
Office of Sponsored Projects, P.O. Box 7726
Austin, TX 73713-7726

8. PERFORMING ORGANIZATION REPORT NUMBER

9. SPONSORING / MONITORING AGENCY NAME(S) AND ADDRESS(ES)

U. S. Army Research Office
P.O. Box 12211
Research Triangle Park, NC 27709-2211

10. SPONSORING / MONITORING AGENCY REPORT NUMBER

40083.5-LS

11. SUPPLEMENTARY NOTES
The views, opinions and/or findings contained in this report are those of the author(s) and should not be construed as an official Department of the Army position, policy or decision, unless so designated by other documentation.

12 a. DISTRIBUTION / AVAILABILITY STATEMENT

Approved for public release; distribution unlimited.

12 b. DISTRIBUTION CODE

13. ABSTRACT (Maximum 200 words)

Semiconductor materials synthesized as oriented nanocrystals or assembled into nanowires and quantum dot solids of a single or multiple materials have technological potential in device fabrication. Our research over the past several years has demonstrated the application of peptides and biological templates to control growth and assemble nanocrystals into potential technologically important materials. The research covered by this grant had three key stages: Selection of Peptides that interacted specifically with a certain material; Using peptides to bind and/or grow nanoparticles or quantum dots; and finally using specific peptide moieties to pattern materials, including heterostructured materials. M13 bacteriophage library screening was used to isolate peptide fusions capable of not only material specific recognition, but directed crystal phase nucleation of some if not all of the semiconductor and magnetic materials studied, including ZnS, CdS, PbS, Co, CoPt, FePt, Fe_2O_3, Fe_3O_4, GaAs, InP, Si and carbon. Virus-semiconductor films were synthesized using the recognition viruses isolated. Genetic engineering encoding the specific peptides was also used to create a viral template to nucleate nanocrystals in an oriented fashion, forming wire-like structures, thus achieving patterning of materials using biological precursors. The nanocrystalline viral nanowires were further transformed to single crystalline nanowires through a heat treatment process.

14. SUBJECT TERMS semiconductor, magnetic, phage, biotemplated, self-assembly, nanomaterials	15. NUMBER OF PAGES 28
	16. PRICE CODE

17. SECURITY CLASSIFICATION OR REPORT UNCLASSIFIED	18. SECURITY CLASSIFICATION ON THIS PAGE UNCLASSIFIED	19. SECURITY CLASSIFICATION OF ABSTRACT UNCLASSIFIED	20. LIMITATION OF ABSTRACT UL

NSN 7540-01-280-5500

Standard Form 298 (Rev.2-89)
Prescribed by ANSI Std. 239-18
298-102

20030714 220

PI: Angela M. Belcher, The University of Texas at Austin
ARO Final Report

" Biomolecular Recognition of Semiconductors and Magnetic Materials to Pattern Quantum Confined and Magnetoelectronic Structures "

Table of Contents

List of Figures and Tables

Statement of Problem Studied

The research in the original proposal had the express purpose of developing radically new techniques for the patterning and interconnection of electronic and magnetic materials on nano length scales in order to design and investigate next generation materials and devices. The approach utilized the inherent self-organizing, highly selective properties of biologically derived molecules. The goal was to radically alter our ability to form and assemble nanoscale electronic and magnetic devices and systems. In particular, we proposed to use proteins to nucleate and pattern useful electronic and magnetic materials. Potential application of these materials included optoelectronic devices such as light emitting displays, optical detectors and lasers; fast interconnects; and nanometer scale computer components. We employed a peptide combinatorial approach to identify proteins that selected for and specifically bound to inorganic nanoparticles such as semiconductor quantum dots. Because nature has not had the opportunity to produce biomolecular interactions with some of the desired materials, we proposed to use phage display libraries to select peptide sequences that would bind to these materials. The library used for the initial experiments had 1.9×10^9 different random sequences and the fused random peptide was displayed on the coat of the phage. The phage display approach provided a physical linkage between the substrate interactions and the DNA that encoded that interaction. Proteins that selected specific inorganic particles were sequenced, cloned and genetically engineered for higher affinity binding. These recognition peptides attached to the particles would act as interconnect sites for conducting polymers or other attaching molecules, with the goal of forming macroscopically ordered addressable storage arrays or circuits.

Summary of Most Important Results

Semiconductor materials synthesized as oriented nanocrystals and/or assembled into nanowires and quantum dot solids of a single material or interveined with different types of materials have technological potential in device fabrication. [1-6] Our research over the past several years has demonstrated the application of peptides and biological templates to control growth and assemble nanocrystals into potential technologically important materials, including heterostructures and superlattices. [7-10] The research covered by this grant had three key stages: Selection of Peptides that interaction specifically with a certain material; The use of such peptides to bind and/or grow nanoparticles or quantum dots; and finally the patterning of such specific peptide moieties in order to pattern materials, including heterostructured mateials.

Specific peptide recogntion and control over material assembly was found through the use of M13 bacteriophage screening used to isolate peptide fusions capable of not only material specific recognition, but directed crystal phase nucleation of some if not all of the semiconductor and magnetic materials studied, including ZnS, CdS, PbS, Co, CoPt, FePt, Fe_2O_3, Fe_3O_4, GaAs, InP, Si and carbon. The peptides isolated from selection experiments were then genetically encoded for expression along the length of a virus, and as such, an engineered viral template was shown to nucleate nanocrystals in an oriented fashion, forming wire-like structures, thus achieving patterning of materials using biological precursors. The nanocrystalline viral nanowires are further transformed to single crystalline nanowires through a designed heat treatment process.

II-VI Semiconductor Materials

Peptide selection and nucleation of ZnS and CdS

Biological selection using the M13 bacteriophage was used to isolate peptide-phage fusions capable of specific recognition and nucleation of zinc sulfide (ZnS) and cadmium sulfide (CdS) nanocrystals. [11] Depending on the growth conditions of bulk phase or nanocrystals, II-VI semiconductors can be crystallized into either zinc blende or wurtzite structure. Zinc blende and wurtzite belong to cubic and hexagonal crystal classes, respectively. Both forms are structurally similar, with the only difference arising from the "staggered" and "eclipsed" positions of the fourth interatomic bond along the (111) chain. [12] Our results, currently being submitted to the *Journal of Materials Chemistry*, have demonstrated that specific interactions with engineered peptides can control nucleated nanocrystal structure for both ZnS and CdS.

Two peptides, A7 and Z8, isolated from different phage combinatorial libraries were successfully identified as consensus motifs for ZnS (Figure 1, Figure 2) . Nucleation studies were performed with A7 and Z8 to determine the peptide's affect on nanocrystal growth. TEM and ED data revealed that the virus constructs were found to control both crystal size and structure of semiconductor nanocrystals synthesized in aqueous solution at room temperature. Most significantly, different engineered peptide-virus constructs were found that directed the specific nucleation of either zinc-blende or wurtzite structure for ZnS nanocrystals. Upon HRTEM analysis of the resultant nanocrystals, two different phases of ZnS were grown in the presence of A7 and Z8 (Figure 3). A7 directed the wurtzite structure crystal phase while Z8 directed the sphalerite crystal phase. Without any size exclusion purification

4

A7		Asn	Asn	Pro	Met		Gln	Asn			
Z8	Val	Ile		Asn		Ala					Leu

Plasmid DNA

Figure 1 (above): N-terminal Peptide sequences A7 and Z8 isolated from ZnS screening with virus combinatorial library. These two sequences were used to nucleate nanocrystals of ZnS

Peptide Insert Structure

Figure 2 (left): Illustratration of the peptide insert structure that is expressed upon phage generation, showing the two libraries used as reported in this research, a 12 mer linear and 7 mer constrained with a disulfide bond.

technique or high temperature synthetic routes, as is the current standard process in traditional inorganic synthesis of such nanocrystals, the A7 peptide synthesized particles with a narrow size distribution near 10%. The Z8 peptide synthesized nanoparticles with a narrow size distribution near 14%, in an aqueous, room temperature environment. Furthermore, when the A7 and Z8 sequences were displayed on the length of the virus protein coat, the same crystal phase control was seen.
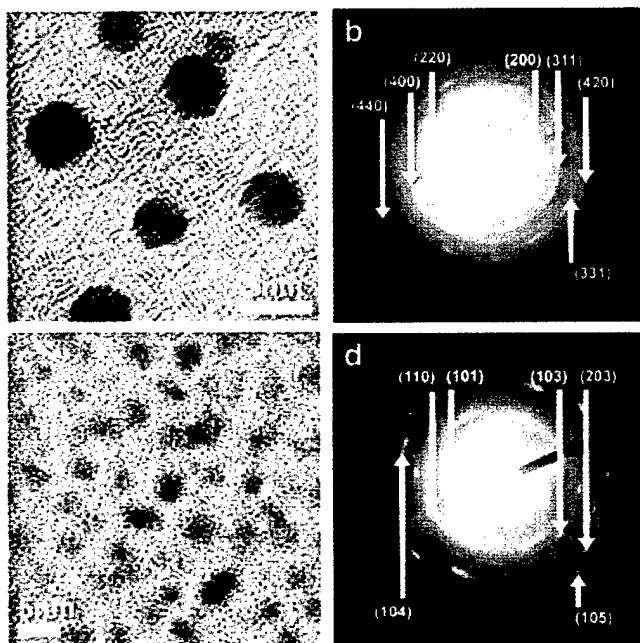
Figure 3 (left): Evidence of nanocrystals influenced by Z8 and A7 viruses. a, HRTEM images showing the lattice spacing of the Z8-directed ZnS nanocrystal. Inset confirms the nanocrystals grown were of the zinc blende crystal phase; b, ED pattern confirming formation of spahlerite ZnS; c, HRTEM images showing the lattice spacing of the A7-directed ZnS nanocrystal. crystal phase; d, ED pattern confirming the nanocrystals grown were of the wurtzite.

A parallel study with CdS was done to identify the peptides J140 and J182 as consensus motifs (Figure 4). Upon HRTEM analysis of the resultant nanocrystals, two different phases of CdS were grown in the presence of J140 and J182, a trend parallel to that seen with ZnS specific phage grown nanocrystals. J140 directed the wurtzite structure crystal phase while J182 directed the zinc blende crystal phase (Figure 5). Without any size exclusion purification technique or high temperature synthetic routes, as is the current standard process in traditional inorganic synthesis of such nanocrystals, the J140 peptide synthesized particles with a narrow size distribution near 13%. The J182 peptide synthesized nanoparticles with a size distribution near 23%, in an aqueous, room temperature environment. While the size distribution for these peptide-directed nanocrystals was not as narrow as seen with the ZnS phage clones, the resultant data shows that the peptide control was applicable to a family of II-VI semiconductor materials.
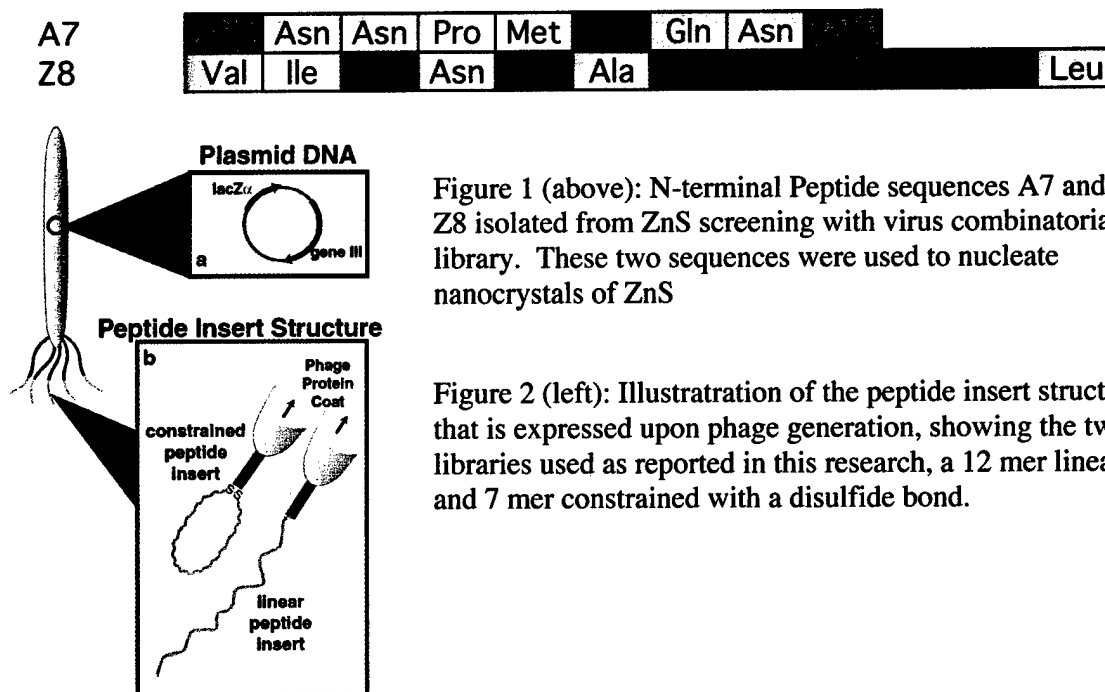

Figure 4: N-terminal Peptide sequences isolated from CdS screening with virus combinatorial library. There two sequences were used to nucleate nanocrystals of CdS
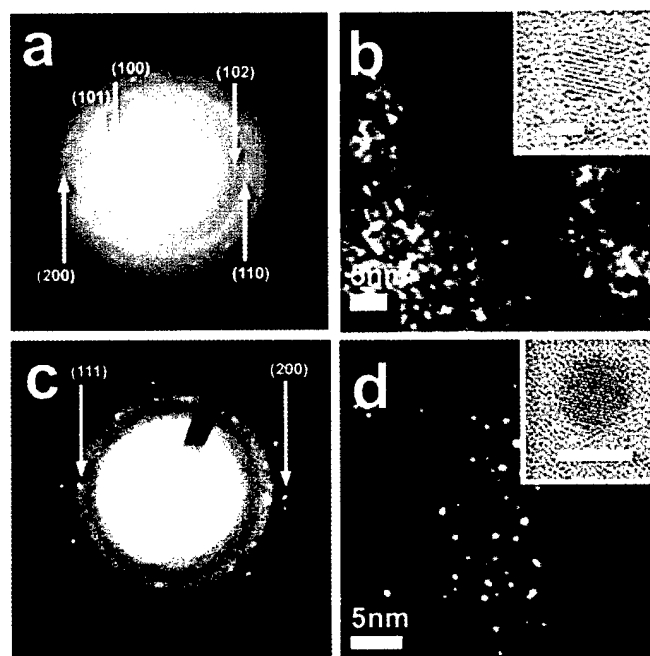
Figure 5: Evidence of nanocrystals influenced by J140 and J182 phage. a,. ED pattern confirming the J140-directed CdS nanocrystals grown were of the wurtzite crystal phase. b, HAADF STEM image at high magnification of J140-directed ZnS nanocrystals. Inset, HRTEM images showing the lattice spacing of the J140-directed ZnS nanocrystal c, ED pattern confirming the J182-directed CdS nanocrystals grown were of the zinc blende crystal phase, with indexing to the (110) and the (200) crystal planes d, HAADF STEM image at high magnification of J182-directed ZnS nanocrystals. Inset, HRTEM images showing the lattice spacing of the J182-directed ZnS nanocrystal.

6

Patterning of ZnS and CdS using Peptide-Engineered Viral Templates

The highly organized structure of M13 bacteriophage was used as an evolved biological template for the nucleation and orientation of semiconductor nanowires, as was reported in the *Proceedings of the National Academy of Sciences*.[9] To create this organized template, successful nucleating peptides were expressed as pVIII fusion proteins along the length of the virus. Phagemid constructs, which contained bacterial plasmid DNA encased in a viral protein coat, were used as the basic building block of the viral wire semiconductor template (Figure 6a). The engineered viruses were exposed to semiconductor precursor solutions, and the resultant nanocrystals that were templated along the viruses to form nanowires were extensively characterized using high resolution analytical electron microscopy and photoluminescence.
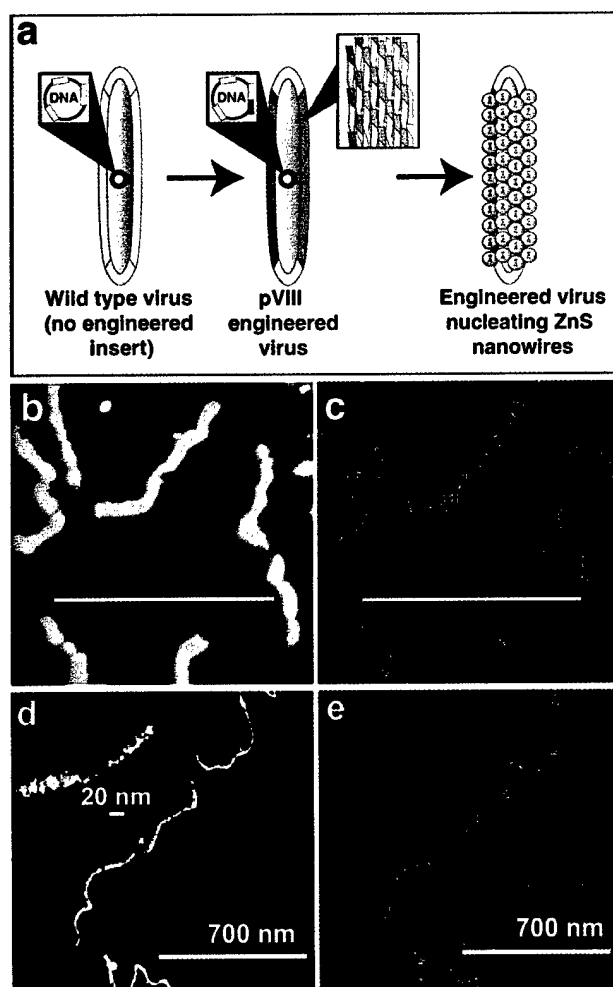
Figure 6: a, Illustration depicting A7 peptide expression on the pVIII protein upon phage amplification and assembly, then subsequent nucleation of ZnS nanocrystals. Call outs depict insertion of the A7 nucleotide sequences, resulting in A7 fusion protein shown as green shaded areas. Also, the call out of the engineered virus shows detail of the wild-type pVIII protein (gray) and the A7-engineered pVIII protein (green) composing the viral coat. b, ADF STEM images showing the morphology of the ZnS-virus nanowires. The ZnS-virus nanowires were 560 nm long and 20 nm wide; c, EDS mapping of S (an identical EDS mapping of Zn was also observed). d, ADF STEM image of viral CdS–virus nanowires. Inset, HAADF image of the framed portion in d. e, corresponding EDS mapping of elements Cd (S mapping resulted in an identical image), scale bar 1 μm.

The ZnS and CdS specific peptides were found to function the same in either of two different fusion constructs, a pIII and pVIII fusion. ZnS nanocrystals were well crystallized on the viral capsid in a hexagonal wurtzite or a cubic zinc blende structure, depending on the peptide expressed on the viral capsid. Electron diffraction patterns showed single crystal type behaviour from a poly-nanocrystalline area of the nanowire formed, suggesting that the nanocrystals on the virus were preferentially oriented with their [001] perpendicular to the viral surface. Peptides that specifically directed CdS nanocrystal growth were also engineered into the viral capsid to create wurtzite CdS virus based nanowires. Lastly, heterostructured nucleation was achieved with a dual-peptide virus engineered to express two distinct peptides within the same viral capsid. CdS and ZnS were then simultaneously nucleated stochastically along the length of the virus wire. This represented a genetically controlled biological synthesis route to a semiconductor nanoscale heterostructure.

Atomic Force Microscopy was used to observe that the engineered A7pVIII phage were slightly different in length and width that the combinatorial library (Figure 7). The size differences arose from the different packaging lengths used in the engineering of the plasmid vector from which protein VIII was incorporated upon virus assembly. This observation and the potential use of such engineered viruses as nano-templates for the organization of crystals into nanowires lead to the idea that wire length could be custom-tailored. A7pVIII constructs were observed to be 560 nm in length compared to wild type and library pIII engineered A7, both of which were 860nm in length. The A7pVIII and Z8pVIII viruses were also visualized by TEM. The AFM images were used to confirm the length scale observed by TEM.
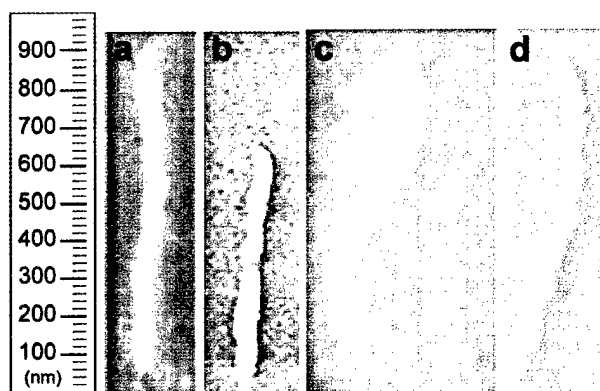
Figure 7: AFM images of the viruses, showing differing lengths depending on how the virus was engineered. The image in **a** shows a pIII A7 engineered virus; **b** shows an A7 pVIII engineered virus; **c** shows a pIII wild type virus; and **d** shows a wild type pVIII virus.

From the detailed study of A7-ZnS and Z8-ZnS complexes, as well as the initial studies performed with J182-CdS and J140-CdS complexes, phage display provided a route to the identification of peptides that could effectively modulate the growth of nanocrystals in aqueous solution under ambient conditions. As such, this method provides a new route to the synthesis of nanocrystals with specified physical characteristics such as size and crystal phase and has the potential to assemble biological II-VI hybrid materials into spatially complex functional mesoscopic electronic and photonic structures. Further refinements of the method can be envisioned to provide a rather general strategy for controlling the crystal formation of other II-VI semiconductors. An attractive feature of the approach is that the peptides can be fused onto other proteins, that, in turn, can provide a template for the assembly of ordered nanocrystals on a variety of size scales. Ideally, using engineered peptides and fusion

proteins may someday allow the construction of spatially complex functional mesoscopic electronic and photonic structures.

The nanocrystalline viral nanowires were further transformed to single crystalline nanowires (Figure 8) through a designed heat treatment process. The single crystalline nanowires were formed by a mechanism of oriented aggregation-based crystal growth in which adjacent nanocrystals on the viruses aggregate and rotate so their structures adopt parallel orientations in three dimensions. Crystal growth is accomplished by removing the underlying viruses at high temperatures and eliminating the interfaces in between two adjacent nanocrystals driven by interface energy minimization. The length of the wire-like viruses can be genetically controlled, and thus our biological route represents the genetic control over the nanowire synthesis.

The mineralized viral wires were then transferred to chemically modified SiOx substrates (wafers or TEM grids). After the viral wires were transferred onto the SiOx substrates, the substrates were annealed at temperatures around a characteristic temperature (Tc) where a large number of smaller nanocrystals were melted. Tc was determined through trial-and-error experiments, and was found to be 400-500 C, depending on the size distribution of the nanocrystals on the virus.

The virus nanowires were found to rapidly transform into single crystalline nanowires (Figure 8 below) within 5 hours due to the high reactivity of the nanocrystals. HRTEM observations show that the nanocrystals in close-proximity and with preferred orientation were aggregated into larger single crystals, driven by the elimination of interface and reducing of the interface energy. The preferred orientation of ZnS nanocrystals on the viral wires, resulting from nucleation directed by fused peptides of uniform conformation on the virus coat, resulted in the formation of larger single crystals on the virus, which consequently led to the formation of single crystalline nanowires. The preferred orientation indicated that a majority of nanocrystals (orientated nanocrystals) shared the similar crystallographic orientation
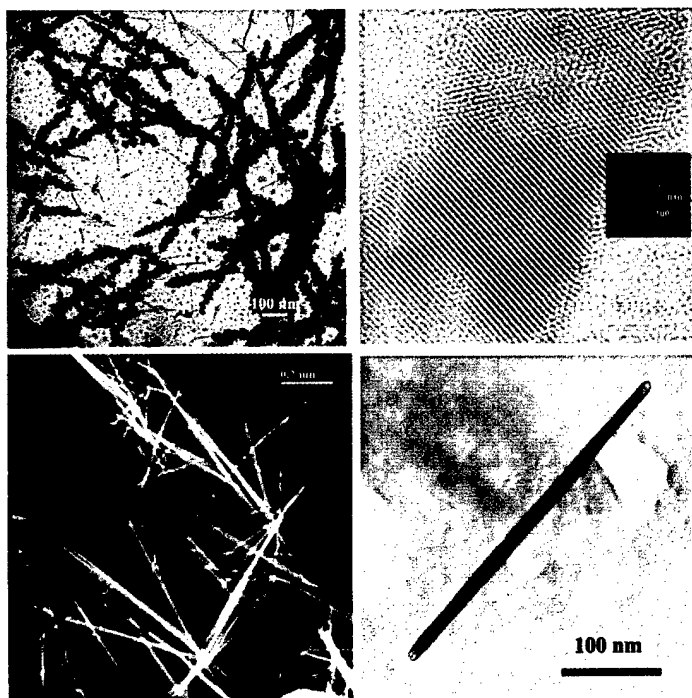

Figure 8: TEM and HRTEM images of single crystal nanowires grown on a viral template followed by a heat treatment.

Molecular Orientation in M13 Phage Nanoparticle Cast Films

Genetically engineered viruses, M13 phage and M13 phage bound with ZnS nanoparticles (ZnS-M13), were used to create cast films on semiconductor substrates. A self-assembled ZnS-M13 film where molecules took an in-plane orientation was obtained on both single crystal and polycrystalline substrates, while the M13 phage cast film, prepared under the same conditions, showed no such molecular orientation. We investigated the film formation process using atomic force microscopy and scanning electronic microscopy. The real space images showed that the order of molecular orientation depends on the concentration of aqueous solutions and the roughness of substrates. The fact that on a smooth substrate, a single ZnS-M13 molecule nucleated the film formation, while on a rough substrate a bundle of ZnS-M13 molecules served as the nucleus, suggests that ordered film formation is driven by capillary meniscus phenomena. Controlling the aqueous solution concentration yielded, for the first time, a highly oriented ZnS-M13 film on an indium tin oxide plate. The ability to control the orientation of virus-based films could lead to new types of hybrid materials in which the components are organized on several length scale.

Molecules and atoms, either singly or as nanometer-sized aggregates, can serve as the elementary units of electronic systems with extremely high component density and configuration flexibility. Most of the previous work[13-15] on the fabrication of array-based devices and the mechanism of molecular orientation focused on small π-conjugated molecules, because they can be controlled easily using traditional technology, such as Langmuir-Blodgett, molecular beam epitaxy techniques, and so on. In contrast, functional biomolecules, especially protein molecules, generally have more and more highly specialized functions.[16-22] To make tiny electronic circuits, much emphasis has been put on mimicking nature ---- finding ways to get inanimate materials to "self-assemble," in a fashion analogous to the way living things grow. Although this area has seen great progress toward the fabrication of a new generation of complex, sophisticated electronic structures, molecular organization and the self-assembly of huge molecules is not completely understood.[23-27]

This work sought to elucidate protein molecular aggregation in a self-assembly system. Aqueous solutions of M13 phage and M13 bound with ZnS nanoparticles were used to prepare cast films on single crystal Si(100) and several polycrystalline substrates. The film formation process was investigated using atomic force microscopy (AFM) and scanning electronic microscopy (SEM). The experimental results revealed the array formation mechanism for M13 phage alone or bound to ZnS-nanoparticles in the cast films. We propose a three-stage film formation model.

We used five substrates in this work: Si (100) single crystal; silicon wafers with a thermally grown oxide layer either 2, 15, or 500 nm thick; and indium tin oxide (ITO) plate. The silicon wafer and commercial ITO plate were purchased from Fluoroware and Metavac, respectively.

The fabrication of the M13 phage and ZnS-M13 as we reported in *Science* in 2002.[29] Aqueous solutions of the M13 phage or ZnS-M13 were cast on the substrates and the solvent was evaporated slowly at room temperature. Atomic force microscopy, AFM (NanoScope IIIa), and scanning electron microscopy, SEM (LEO1530), were used to characterize the film structure.

Nucleation of the M13 phage and ZnS-M13 films in the early stages of film formation were easily seen with AFM. Figure 9 shows a typical AFM image of the boundary area between a Si(100) substrate and the cast film of M13 (a) or ZnS-M13 (b). Early in the film formation,

M13 molecules adsorb on the substrate randomly and link with each other in a branch pattern. ZnS-M13 molecules, however, adsorb on the substrate and remain separate. High-resolution AFM images of the films (Fig.10) show the detailed molecular adsorption characteristics of M13 and ZnS-M13 molecules on the substrate. The length and width of the branched phage and rod-like phages, shown as a and a' in Fig. 10 (a) and (b), are about 880 nm and 6 nm, respectively—consistent with the length and diameter of individual M13 molecules. Our previous work[29] demonstrated that one ZnS-nanoparticle bound at the end of M13 through pIII is about 2-3 nm in diameter. The sphere observed at the end of the rod-like phage may be a ZnS cluster formed from five ZnS nanoparticles bound with the M13; its size, ~15nm, is consistent with that of multiple ZnS nanoparticle aggregates.

These results suggest that M13 phage molecules are laid down alone on the substrate and link to each other randomly. The high affinity of phage for other phage is the basis for film formation. On the other hand, ZnS-M13 molecules adsorb on the substrate surface individually and tend to stack on top of each other. The difference between M13 phage and ZnS-M13 adsorption behavior may arise from differing capillary effects. The ZnS forms a relatively small, roughly spherical cluster at one end of the M13 that is more strongly affected by the capillary meniscus phenomenon; this results in a nucleation pattern very different from that of M13.

In SEM, Figure 11, we find noteworthy the separate ZnS-M13 nuclei observed in a very large area, typically extending to a few micrometers. These nuclei are aligned along the direction of water flux and are the basis of a highly molecularly oriented ZnS-M13 film. We conclude that the molecularly oriented nucleation is induced by the ZnS-nanoparticles; that is, their presence creates a molecular template in the first stage of film formation. However, we know that the ZnS-M13 phage nucleation is not due to molecular epitaxial growth on Si (100) because the molecular orientation does not reflect the crystalline features of that substrate. The nucleation may originate from interactions between ZnS nanoparticles and water flux during solvent evaporation. These results suggest that nucleation must be molecularly oriented to yield an ordered ZnS-M13 film. Such an ordered molecular template might be obtained on a polycrystalline substrate. Also visible in Figure 11 is the variation in orientation with film thickness. The molecular template determines the orientation of the next ZnS-M13 molecules, but the molecular orientation disintegrates where the film is thick, perhaps because the slender M13 phage, like linear molecules, tends to assume a nematic bulk crystal structure.

To clarify whether ZnS-M13 molecules nucleate based on molecular orientation on a polycrystalline substrate, as well as on the Si(100) single crystal surface, we cast 10% and 25% ZnS-M13 aqueous solutions on SiO_2 layers covering a Si(100) surface. The SiO_2 layers were 2, 15, or 500 nm thick. Figure 12 shows AFM images of ZnS-M13 nuclei adsorbed on the SiO_2 layers at both concentrations. The results are summarized in Table 1. At 10% concentration, ZnS-M13 molecules align and order along the water flux direction on 2 nm and 15 nm thick SiO_2 layers, but not on the 500 nm layer. For the 25% concentration, ZnS-M13 molecules nucleate even on the 500 nm SiO_2 layer in a molecular "bundle" about 900 nm long and 40 nm wide. On the other hand, we saw no ordered nuclei for the molecular bundle on the 2 nm and 15 nm SiO_2 layers at 25% concentration.

Rigid backbone polymers forming liquid crystals above a certain critical concentration have been widely reported.[30-34] Generally, between linear molecules, the molecular interaction perpendicular to the molecular axis is stronger than that parallel to the molecular axis. At high solvent concentrations, the linear molecules tend to bundle together; under these conditions, molecules show a high degree of axial orientation normal to the molecular longitudinal axes and

a low degree of orientation in the molecular planes around the longitudinal axes. ZnS-M13 molecules appear to orient similarly to those linear molecules. At 25% concentration, the ZnS-M13 formed liquid crystals in solution, and the crystallized molecular bundle adsorbed on the substrate as a nucleus.

Our results demonstrate that ZnS-M13 molecules nucleate in an orderly fashion on both polycrystalline substrates and Si(100). Variations in the nucleation behavior, depending on concentration and substrate conditions, suggest a capillary force effect between the ZnS nanoparticles and the water during evaporation.

Two-dimensional crystal nucleus formation is governed by attractive lateral capillary forces between particles partially immersed in a liquid layer.[35-40] These interactions are important across a very wide range of particle sizes from 1 nm to 1 mm. Particle dispersion depends initially upon the nature of the substrate surface. When the liquid layer is thinned by solvent removal, particle self-assembly is triggered, finally yielding a hexagonally close-packed array. A theoretical study[23] on capillary meniscus interaction between colloidal particles attached to a liquid-fluid interface demonstrated that for both spherical and cylindrical particles, the energy of capillary interaction is attractive and long-range. But in the case of more than two cylinders, the capillary interaction is not additive pair-wise, and many-body interactions become significant. The self-assembly phenomenon is particularly marked when the solvent thickness is comparable to the diameter of the spherical particles.[39-40]

In this work, we made our films using the casting method; the films formed by water evaporation in about 3 days at room temperature. We note that the ZnS nanoparticles not only change the molecular interaction of the M13 phage but also lead the nucleation. Partially immersed ZnS nanoclusters will adsorb on the substrate along the direction of flux. Because the self-assembly driven by capillary forces is most favored when the solvent thickness is comparable to the particle size, ZnS-M13 nucleates in individual molecules on a smooth surface, such as Si(100) with a <15 nm thick SiO_2 overlayer. But a high concentration condition (namely, a molecular bundle) is required for nucleation on a rough substrate.

The film formation mechanism, therefore, can be described by a three-stage model shown in Scheme 1. In the first stage, nucleation results from the capillary force acting on the ZnS clusters. The second stage of film formation is crystal growth. The first ZnS-M13 molecules act as a template in the second stage and lead other molecules to adsorb in the same pattern by molecular interaction, inducing a wide range molecular orientation. Thus the molecules orient even on a polycrystalline substrate. The final stage is anchoring of the ZnS-M13 molecules, as in other liquid crystals.[41,42] We note that, in contrast with the substrate dependence of molecular orientation in traditional film growth techniques, in-plane molecular orientation of very large molecules can be achieved via a nanoparticle template using lateral capillary force. We expect that this strategy for biomolecular orientation can be employed on various substrates and for films covering very large surfaces.

By controlling the aqueous solution concentration, a high quality molecularly oriented cast ZnS-M13 film was achieved on ITO coated glass substrates. Figure 13 shows the AFM image of the ZnS-M13 film prepared at 25% concentration. The rod-like shape is about 880 nm long and its diameter about 7 nm, in good agreement with the molecular length of the ZnS-M13. The results reveal that the ZnS-M13 molecules orient parallel to the ITO plate in the film and share the same positional long-range ordered structure. The molecularly oriented range extends to a few micrometers. We therefore anticipate application of the films in, for example, photonic materials and microelectronics with novel properties.

Our results demonstrate d that ZnS nanoparticles b ound with M13 form ordered molecular nuclei, while M13 alone does not. The nucleation occurred not by molecular epitaxial growth but by capillary meniscus phenomena. We propose a new three-stage model for film formation. In the first stage, molecular adsorption is induced by the capillary force acting on ZnS-nanoparticles. The long axis of ZnS-M13 lies parallel to the substrate surface and is aligned along the direction of the water flux caused by evaporation. This creates a molecular template over a large area. In the second stage, other molecules adsorb on the molecular template. The third stage is the anchoring that occurs in the film between the ambient air and the ZnS-M13 interface, due to the thread-like M13 molecule's liquid crystal characteristics.
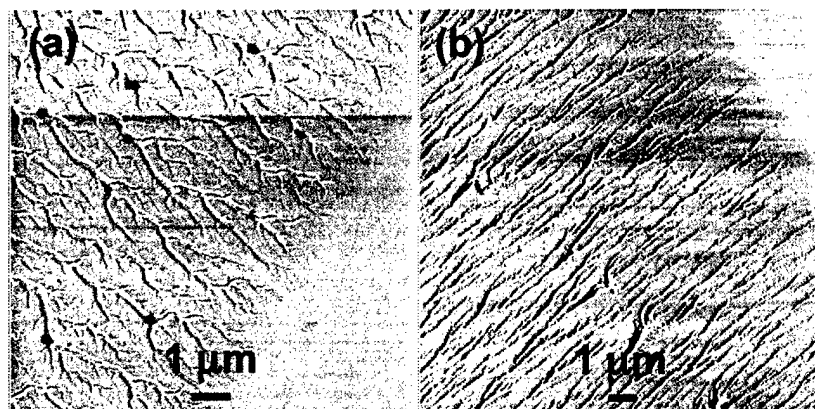

Figure 9. AFM images of the boundary area between the ZnS-M13 (a) and M13 (b) films and Si(100) surfaces.
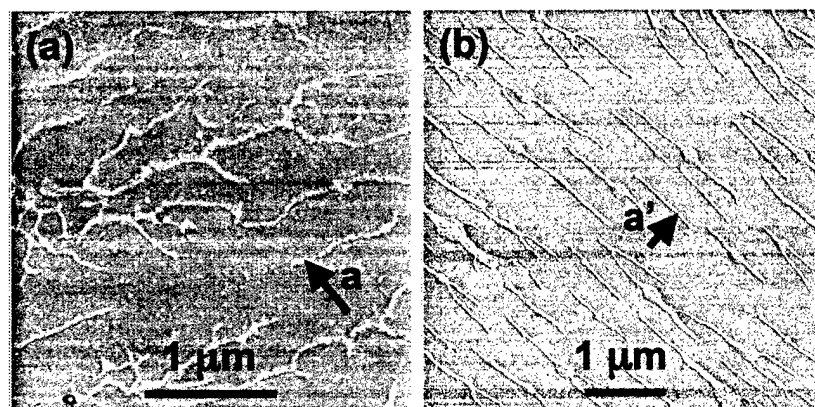

Figure 10. Enlarged AFM images of the M13 and ZnS-M13 molecules adsorbed on Si(100).
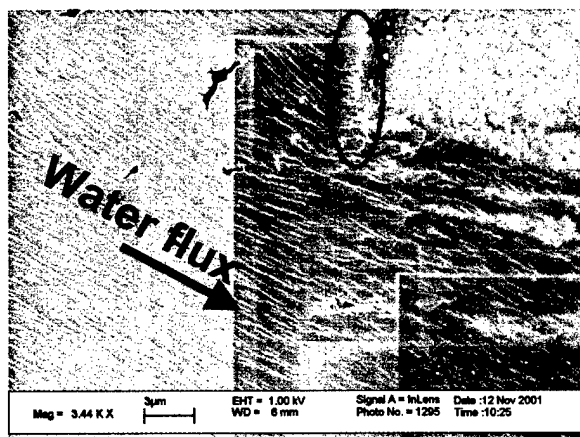
Figure 11. SEM image of ZnS-M13 films cast on Si(100).

13
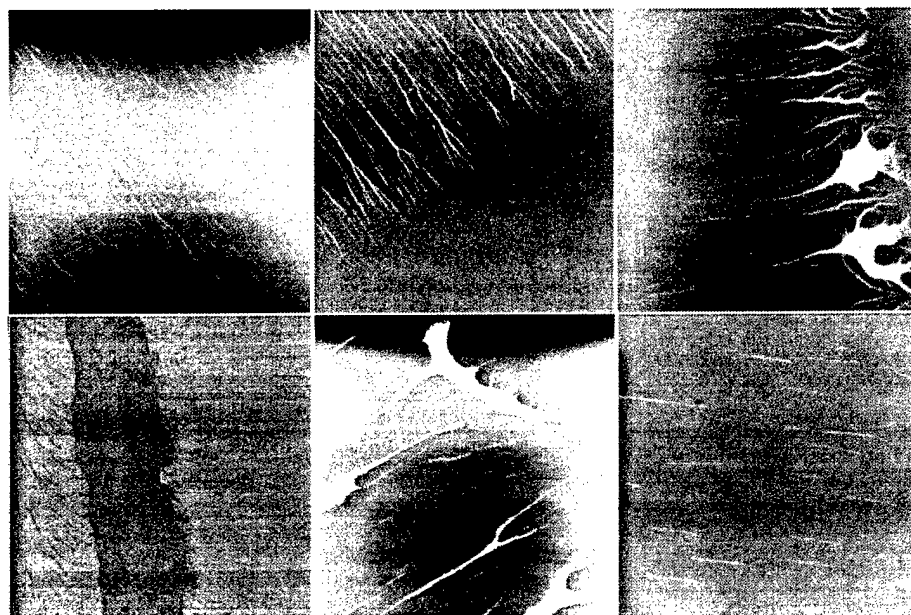
Figure 12. AFM images of ZnS-M13 films cast on SiO$_2$ layers with thicknesses of 2 (a), 15 (b) and 500 nm (c).
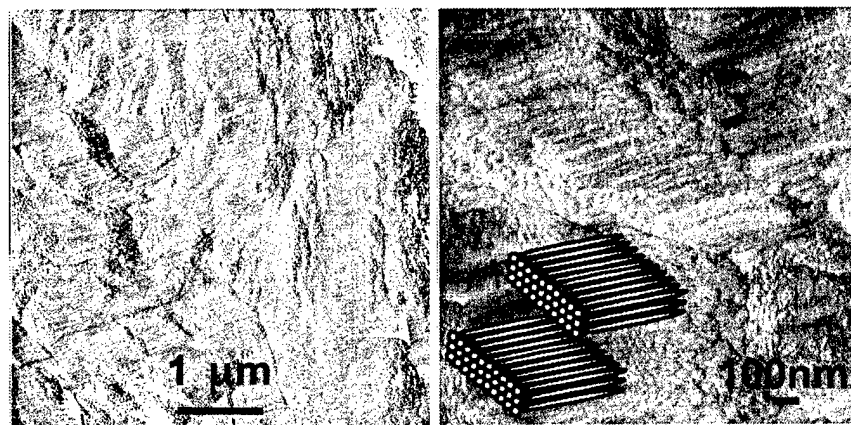
Figure 13. AFM image of the ZnS-M13 film cast on an ITO plate.

Concentration	12±1 mg/ml	30±1 mg/ml
Si(100)	◎	✕
SiO2 (2 nm)	◎	✕
SiO$_2$ (15 nm)	△	✕
SiO$_2$ (500nm)	✕	◎

Table 1. Effects of the concentration of aqueous solution and substrate surface on the nucleation of ordered structures.

◎ form good oriented nucleation
△ form partially oriented nucleation
✕ form randomly oriented nucleation

14

Main intermolecular reaction:
(linear molecular interaction
and interaction between
Zn²⁺ and S²⁻ ions)

Substrate

Step 3:molecular dislocation

Water Evaporation

flux

Substrate

Step 1: Nucleation by capillary force
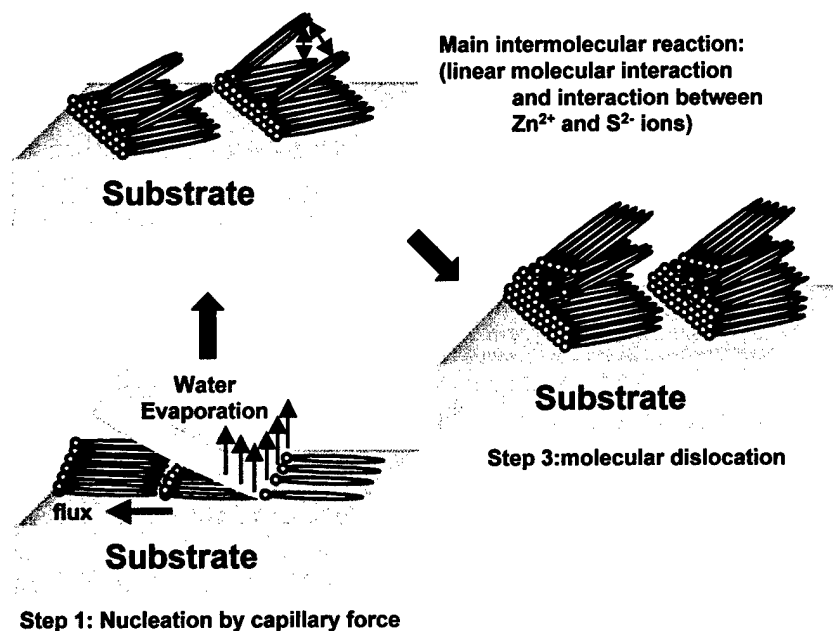
Scheme 1. A proposed 3-stage formation model for ZnS-M13 molecular orientation.

Synthesis and assembly of nanocrystals on peptide functionalized surface

A7 Peptide Nucleation of ZnS. We tested the ability of synthetic A7 peptides, that is, peptide independent from the phage virus on which it was discoverednot attached to phage, to control the structure of ZnS.[43]

A7 peptide, which specifically selected and grew ZnS crystals when attached to the phage, was applied to form a functionalized surface on gold substrate that can direct the formation of ZnS nanocrystals from solution. A process that is used to prepare self-assembled monolayer (SAM) was employed to prepare an A7 functionalized surface.[44-48] To investigate the ability and selectivity of A7 in the formation of ZnS nanocrystals, different kinds of surface with different surface chemistry on the gold substrate are interfaced with ZnS precursor solution with $ZnCl_2$ and Na_2S as ZnS source and CdS precursor solution with $CdCl_2$ and Na_2S as CdS source, respectively.

Field-emission SEM/EDS was used to characterize the crystals formed on different surfaces. From the detailed SEM results summarized below, the ZnS crystals formed on A7-related surface are 5 nm, while the CdS crystals formed on A7-related surface are about 1 -3 microns (Figures 14, 15). And the CdS crystals formed on A7-related surface can also be formed on amine-only surface. Therefore, we can conclude that the A7 peptide can direct the formation of ZnS nanocrystals but can not direct the formation of CdS nanocrystals.

Control surfaces, including a blank Au surface and a 2-mercaptoethyamine self-assembled monolayer (SAM) on the gold substrate, were not able to induce the formation of ZnS and CdS nanocrystals (Figure 16). Only in very few places, ZnS precipitates are found (a). $[Zn^{2+}]=[S^{2-}]=1 \times 10^{-3}$ M. For the CdS system, sparsely distributed 2 microns CdS crystals were observed and thought to be normal precipitation at the given concentration ($[Cd^{2+}]=[S^{2-}]=1 \times 10^{-3}$ M).

15
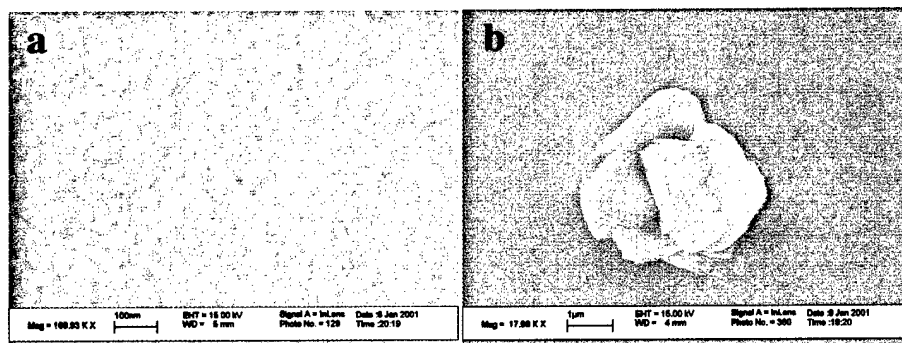
Figure 14. A7-only surface directed the formation of 5 nm ZnS nanocrystals but not the CdS nanocrystals (a) ZnS nanoparticles (b) large CdS precipitation
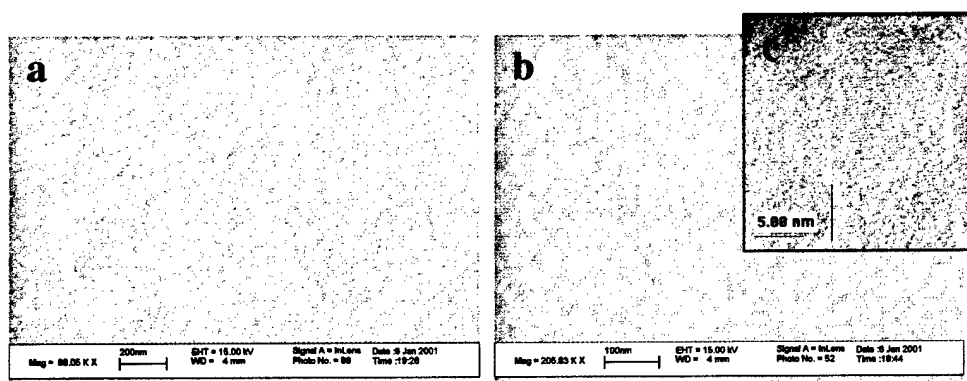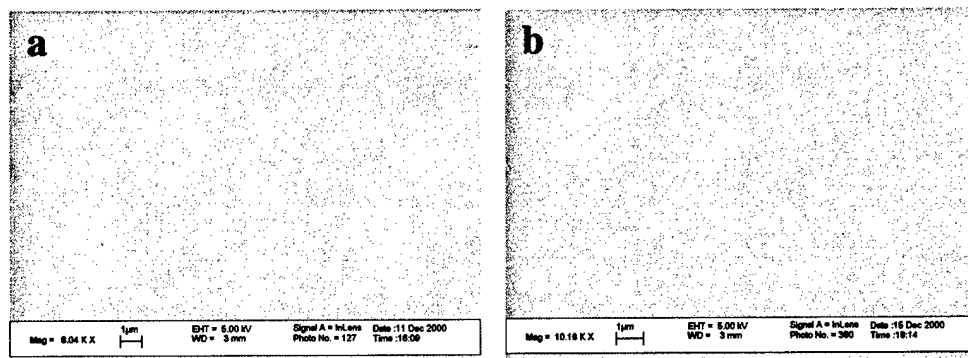

Figure 15. A7-amine surface can direct the formation of 5 nm ZnS nanocrystals (a, b & c) but not CdS nanocrystals.

Figure 16. Typical SEM morphology on control surface-1, blank gold, after being aged (a) in the ZnS solution for 70 h. (b) in the CdS solution for 70 h. No crystals were observed in either control.

16

Magnetic Materials: Co, CoPt and FePt

Using the high temperature scheme developed by Alivisatos and co workers,[49] we synthesized and characterizes magnetic nanoparticles (Figure 17). These nanoparticles were used as substrates for peptide selection using phage display. Consensus peptide sequences for Co, CoPt and FePt were all successfully found.
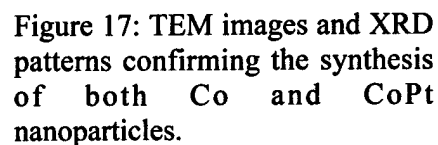
Figure 17: TEM images and XRD patterns confirming the synthesis of both Co and CoPt nanoparticles.

The specificity of Co specific peptide was tested for affinity to bind Co nanoparticles versus Si, using a wild type clone and a random clone as a control. The graph below shows that the Co clone binds Co and has little affinity for Si crystals. The graph in Figure 18 shows that wild type and the random sequence do not have an affinity For Co nanocrystals.

Figure 18: Graph of Co specific peptide binding affinity towards Co

17

Peptide directed growth of magnetic materials.

The most significant work was the ability to grow these magnetic materials at room temperature using the peptides selected. Preliminary results show that we can successful grow hcp 10 nm Co particles and L10 FePt and CoPt 2 nm particles at room temperature! The CoPt and FePt nanoparticles are very well crystallized and were grown in high density (Figure 19). The Co particles were less crystallized, less mono dispersed and were grown in a lower density (Figure 20). We are just starting to study the magnetic properties of these nanoparticles. [50]
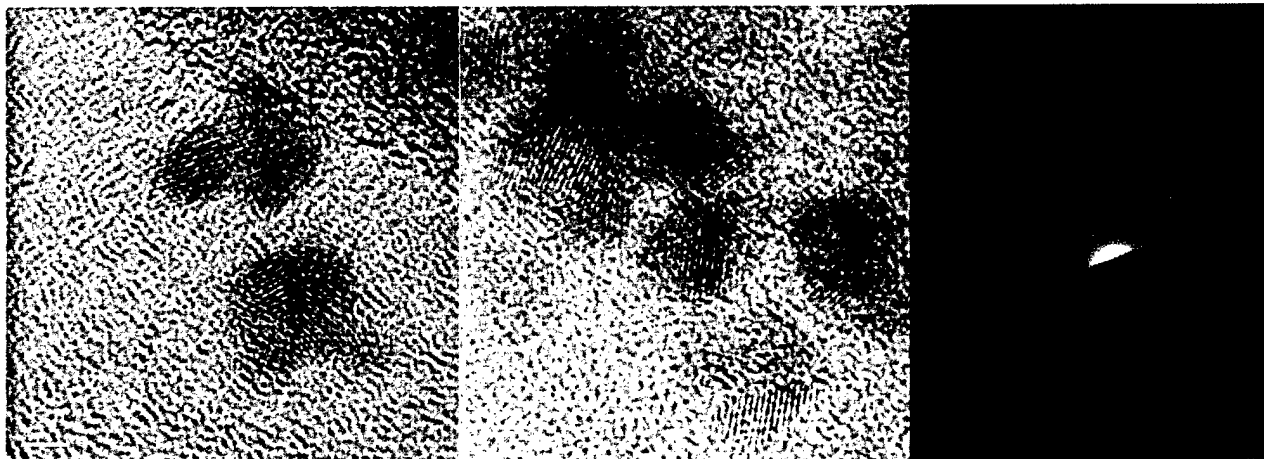

Figure 19: TEM lattice images and electron diffraction of peptide induced nucleation of FePt nanoparticles
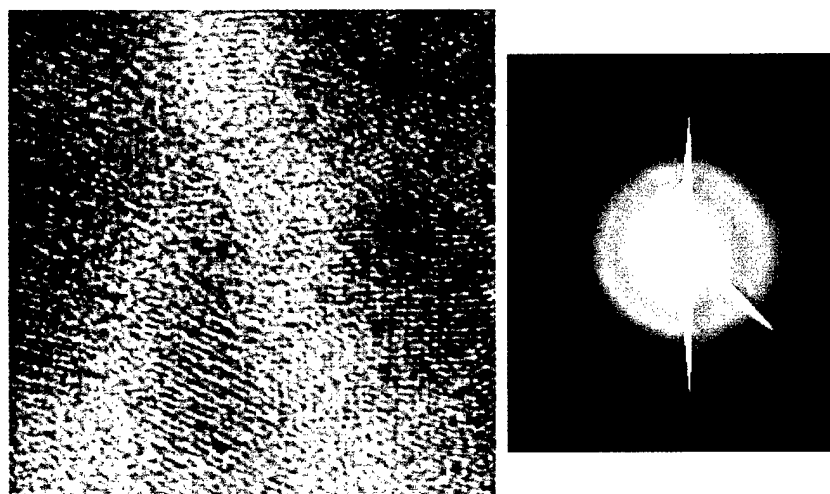

Figure 20: TEM and lattice image of peptide-induced nucleation of hcp Co particles.

18

Carbon nanotubes and graphite

We selected peptides that bind to graphite and to Professor Richard Smalley's HIPCO processed carbon nanotubes. We have come to consensus sequence for both graphite and carbon nanotubes. We made synthetic peptides based on these sequences and tested their specificity. Based on TEM, AFM and fluorescence microscopy peptide selected for carbon nanotubes are able to bind to carbon nanotubes. Peptides selected for graphite have a high affinity for graphite substrates. However these graphite specific peptides do not show a high affinity for nanotubes. Carbon nanotube specific peptides do show some affinity for graphite. Below are TEM and fluorescence microscopy preliminary data showing carbon nanotube peptides binding to a sample of HIPCO processed nanotubes. For the fluorescence microscopy image the peptide was synthesized with a biotin label and FITC streptavidin was used to tag the carbon nanotube specific peptide. For TEM studies gold labeled streptavidin was used to tag he carbon nanotube specific peptide.
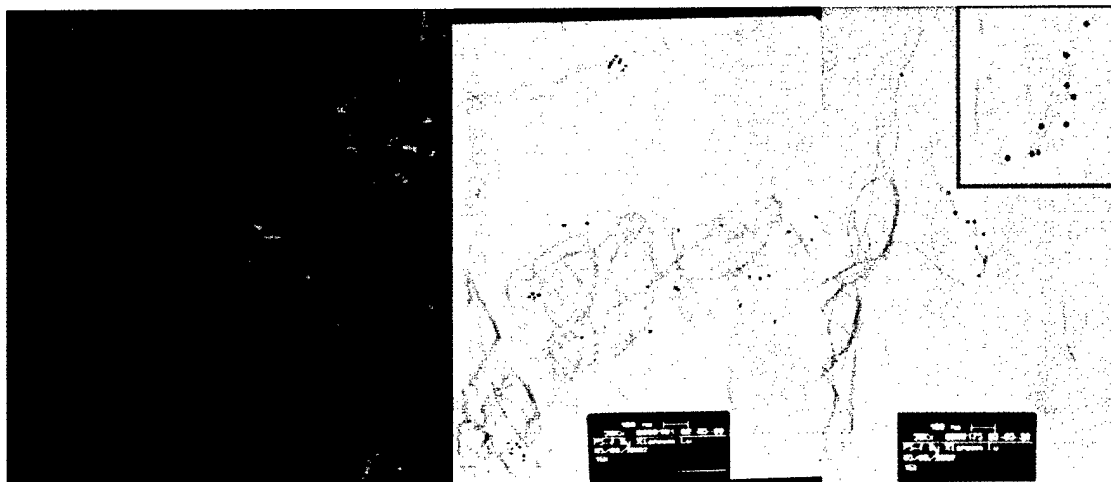

Figure 21: (a) Carbon nanotubes labeled with a FITC fluorescent dye, attached via a specific biotinylated peptide. (b) TEM images of gold labeled streptavidin attached to carbon nanotubes via a selected specific peptide.

Silicon

Biopanning was initiated on silicon substrates of two distinct dopant concentrations. The substrates were {100} Silicon p-type (boron) with a resistivity of 13.5Ω-cm with two types of dopant implants 1) phosphorous implant with a dose of $1.00E14/cm^2$ at 10KeV and 7 deg. tilt and 2) BF_2 implant with a dose of $2.00E13/cm^2$ at 5 KeV and 7 deg. tilt. Before each biopan the native oxide was removed by etching in 40:1 HF for 2min. The substrates were then rinsed in DI and air dried. The biopanning began 5-10 minutes after the HF dip so the silicon substrate should have a hydrogen passivation layer.

Preliminary biopanning, second round, performed on n- and p- doped silicon substrates reveal peptide distributions indicating preferential binding between positively and negatively charged R groups. Positively charged R groups of Lysine, Arginine, and Histidine had a 16.82% occurrence after the third round of biopanning on the n- type silicon substrate. These same amino acids had a 9.72% occurrence on the p- type silicon substrates. The negatively charged R groups of Aspartate and Glutamate were distributed 5.61% for the n- type substrate and 6.94% for the p- type substrate. Of particular interest in the negatively charged amino acid group is glutamate which was distributed at 4.17% on the p- type substrate and only 1.87% on the n- type substrate. Major differences were also observed in the polar uncharged R groups with serine, threonine, and proline binding with higher distributions on the n- type substrate, and Asparagine and Glutamine binding with higher distributions to the p- type substrate. Two peptides sequences are shown below one reach for n- and p- doped silicon (light gray represent negative charged amino acids, dark Grey represent positive charges amino acids.

| p-Si | Glu | Ala | Gln | Ser | Thr | Tyr | Glu | Leu | Arg | Ala | Glu | Asn |
| n-Si | Ser | Pro | His | Pro | Ile | Tyr | Lys | His | Thr | Tyr | Gln | Arg |

Further screening and condition deviations during screening are being investigated with Silicon substrates.

Iron oxides

Phage were selected that specifically bind to iron oxide nanoparticles.[7] Phage clone F11 has been shown to bind 4 nm and 13 nm Fe_3O_4 nanoparticles as discrete particles. The TEM image shown in Figure 22 illustrates that the F11 peptides acts as a capping agent and prevents the nanoparticles of Fe_3O_4 from binding to each other. The figure on the left shows aggregation in the absence of F11, and the image on the right shows the individual nanoparticles in the presence of F11. Figure 23 is an AFM image of the F11 clone binding 13 nm Fe_3O_4 nanoparticles. This binding specificity will be further investigated. The placement of these biomolecule-Fe_3O_4 nanoparticles are being explored. We were also able to monitor the pH reversible binding of F11 clone to Fe_3O_4 nanoparticles in fluids using AFM tapping in liquid (Figure 24 below).

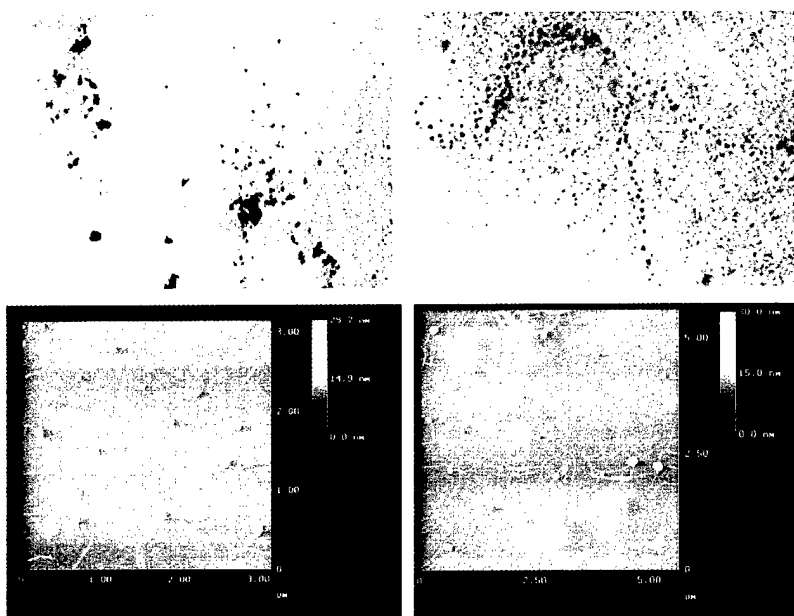Figure 22. TEM image of (Left) Aggregates of Fe_3O_4 formed in absence of phage (Right) Phage bound to Fe_3O_4 nanoparticle organized into wire-like rows.

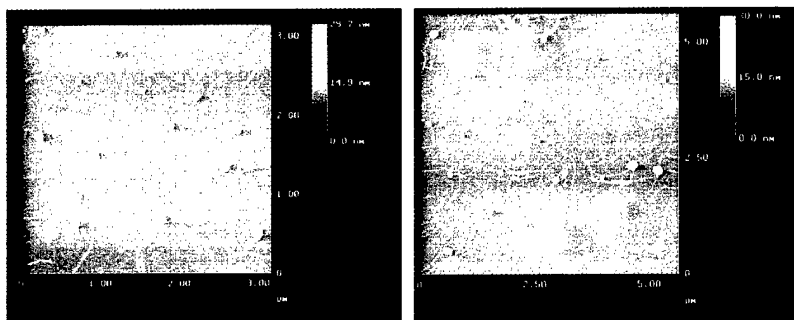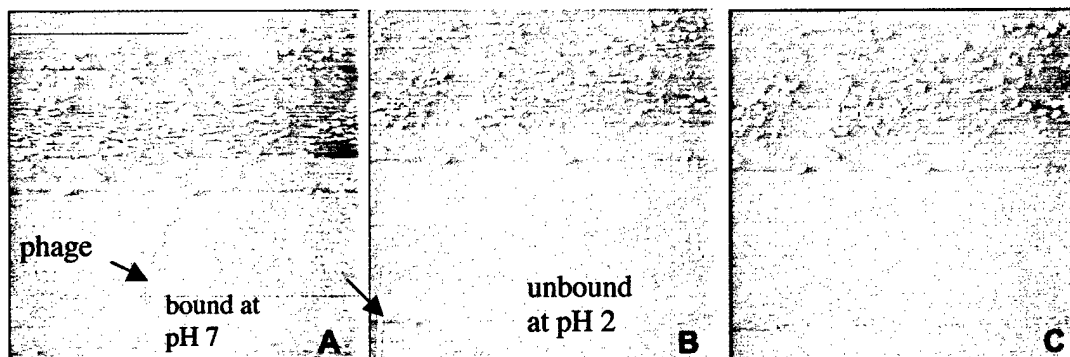Figure 23. AFM of the clone F11 showing attachment of 13 nm Fe_3O_4 to primarily one end of the phage.

phage
bound at pH 7   A
unbound at pH 2   B
C

Figure 24: AFM inages monitoring the pH reversible binding of F11 clone to Fe_3O_4 nanoparticles in fluids.

<u>Binding Experiments</u>: binding experiments were performed separately with magnetite and hematite, then comparatively in order to find the relative binding order among clones isolated after six rounds of biopanning. The clones JH-127, JH-77, JH-86, and JH-78 were magnetite specific (Fe_3O_4) and the clones JH-93, JH-99 and JH-95 were hematite specific (Fe_2O_3).
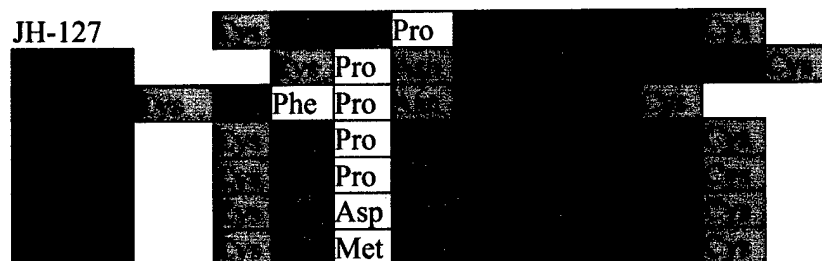
In the binding experiment, a constant amount of a material specific clone was added to the fresh substrate (Fe_2O_3 or Fe_3O_4). The clones were interacted with the substrate for two hours in order to allow equilibrium to be reached. After two hours, the phage solution was removed and the substrate was rinsed. Each phage solution was then titered in duplicate in order to determine the relative binding order, along with the error within the titering measurement. The results of the binding experiment are shown in the graphs for each material in Figure 25, with the average PFU of the eluted phage plotted on the y-axis..
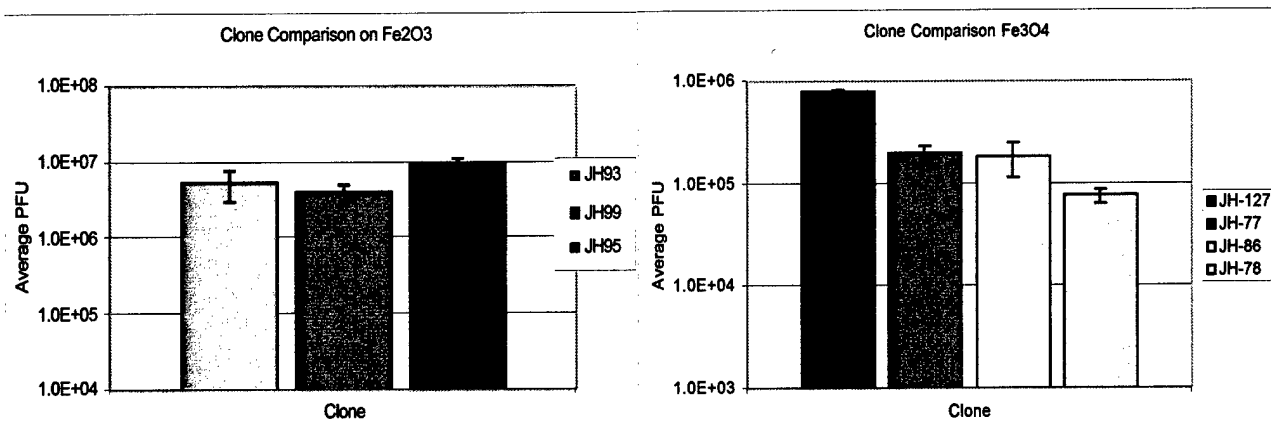
Figure 25: (left) Comparison of binding affinity of Fe_2O_3 specific clones on Fe_2O_3. (right) Comparison of Fe_3O_4 specific clones on Fe_3O_4

A similar experiment was done in order to determine the degree of specificity of Fe2O3 clone binding to the hematite surface versus the magnetite surface. These experiments were done using a constant mass of the two powders. Constant mass was used due to the similarities in densities and particle sizes in the hematite and magnetite used, therefore constant mass should mean that a constant amount of surface area would be available for binding. In the following experiment, 2.1 mg of magnetite and hematite

were added to microcentrifuge tubes before adding 750 μL of TBST and 3x10^9 PFU of the Fe2O3 clone JH-95. Under these conditions, it was found that the JH-95 clone binds better to the magnetite surface than to the hematite surface but not by more than an order of magnitude (see graph below, Figure 26).

Fe2O3 Clone Specificity:
magnetite versus hematite
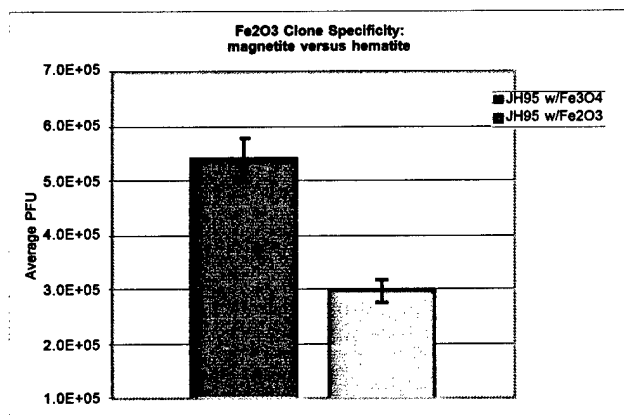
Figure 26: Magnetite specific clone study on hematite

The reverse experiment was done in order to determine the degree of specificity of Fe$_3$O$_4$ clone binding to the hematite surface versus the magnetite surface. Under the conditions used, it was found that both the JH-127 and the JH-78 clone bind better to the magnetite surface than to the hematite surface by less than an order of magnitude for JH-127 and by almost an order of magnitude for JH-78. According to this experiment, JH-127 binds with greater density but with less specificity than JH-78. This experiment is being duplicated using larger hematite and magnetite particles in order to determine whether particle size plays a role in the specificity of binding.

List of Publications

Peer-reviewed Journals

Mao, Chuanbin; Qi, Jifa; and Belcher, Angela M. **Building quantum dots into solids with well-defined shapes**, In Press, *Advanced Functional Materials*, 2003

Mao, Chuanbin; Flynn, Christine E.; Hayhurst, Andrew; Sweeney, Rozamond; Qi, Jifa; Georgiou, George; Iverson, Brent; and Belcher, Angela M. **Viral assembly of oriented quantum dot nanowires** . *Proc. Natl. Acad. Sci. USA* 2003 100: 6946-6951.

Lee, Seung-Wuk; Lee, Soo Kwan; Belcher, Angela M.. **Virus-based alignment of inorganic, organic, and biological nanosized materials.** *Advanced Materials* (Weinheim, Germany) (2003), 15(9), 689-692.

Lee, Seung-Wuk; Wood, Bryant M.; Belcher, Angela M.. **Chiral Smectic C Structures of Virus-Based Films.** *Langmuir* (2003), 9(5),1592-1598.

Lee, Seung-Wuk; Mao, Chuanbin; Flynn, Christine E.; Belcher, Angela M.. **Ordering of quantum dots using genetically engineered viruses.** *Science* (Washington, DC, United States) (2002), 296(5569), 892-895.

Seeman, Nadrian C.; Belcher, Angela M.. **Emulating biology: building nanostructures from the bottom up.** *Proc. Natl. Acad. Sci. USA* (2002), 99 (9, Suppl. 2), 6451-6455.

Whaley, Sandra R.; English, D. S.; Hu, Evelyn L.; Barbara, Paul F.; Belcher, Angela M.. **Selection of peptides with semiconductor binding specificity for directed nanocrystal assembly.** *Nature* (London) (2000), 405(6787), 665-668.

Non-Reviewed Journals and Conference Proceedings

Belcher, Angela M.; Gooch, Erin E. **Protein components and inorganic structure in shell nacre.** Biomineralization (2000), 221-249.

Whaley, Sandra R.; Belcher, Angela M.. **Borrowing ideas from nature: peptide-specific binding to gallium arsenide.** *Materials Research Society Symposium Proceedings* (2000), 599(Mineralization in Natural and Synthetic Biomaterials),189-199.

Other Papers Presented at Meetings

80

Manuscripts Submitted

Flynn, Christine E.; Mao, Chuanbin; Hayhurst, Andrew; Williams, Julie L.; Georgiou, George; Iverson, Brent; and Belcher, Angela M. **Synthesis and Organization of Nanoscale II-VI Semiconductor Materials Using Evolved Peptide Specificity and Viral Capsid Assembly.** Submitted to *Journal of Materials Chemistry*, 2003

Ni, J., S.W. Lee, J.M. White and A.M. Belcher, **Molecular Orientation of ZnS Nanocrystal Modified M13 Viruses on Silicon**, submitted to *Journal of Polymer Science*, Polymer Physics, 2003.

Brian D. Reiss, Chuanbin Mao, Daniel J. Solis, Rozamond Y. Sweeney, Katherine S. Ryan, Anuj Aggarwal, Thomas Thomson, and Angela M. Belcher. **Biological Routes to Metal Alloy Ferromagnetic Nanostructures**, Submitted to *Nature Materials*, 2003.

Technical Reports Submitted to ARO

3

Participating Scientific Personnel

Angela Belcher, Principal Investigator

Chuanbin Mao, PostDoctoral Fellow

Esther Ryan, PostDoctoral Fellow

Sandra Whaley, Graduate Student, earned Ph.D. December 2001

Christine Flynn, Graduate Student, earned Ph.D. May 2003

Erin Gooch, Graduate Student

Kiley Miller, Graduate Student

Ioana Pavel, Graduate Student

Harshal Gupta, Undergraduate Research Assistant

Jennifer Hsing, Undergraduate Research Assistant

Julie Williams, Undergraduate Research Assistant

Alicia Gutierrez, Undergraduate Research Assistant

Report of Inventions

Belcher, Angela M.; Lee, Seung-wuk. **Nanoscaling ordering of hybrid materials using genetically engineered mesoscale virus.** PCT Int. Appl. (2003), 70 pp.

Belcher, Angela M.; Smalley, Richard E.; Ryan, Esther; Lee, Seung-Wuk. **Biological control of particle size of nanoparticles from semiconductors and carbon.** PCT Int. Appl. (2003), 160 pp.

Belcher, Angela M.; Flynn, Christine E. **Biological control of nanoparticle nucleation, shape and crystal phase** PCT Int. Appl (2002)

Belcher, Angela M. **Molecular Recognition of Materials,** UTA Patent No. B-2457, 1049.

Bibliography

1. A. P. Alivisatos. *J. Phys. Chem. B,* 1996, **100**, 13226-13239.

2. B. O. Dabbousi, J. Rodriguez-Viejo, F. V. Mikulec, J. R. Heine, H. Mattoussi, R. Ober, K. F. Jensen & M. G. Bawendi. *J. Phys. Chem. B,* 1997, **101**, 9463-9475.

3. A. L. Efros & M. Rosen. *Annu. Rev. Mater. Sci.,* 2000, **30**, 475.

4. J. Nanda, S. Sapra, D. D. Sarma, N. Chandrasekharan & G. Hodes. *Chem. Mater.,* 2000, **12**, 1018.

5. C. B. Murray, C. R. Kagan & M. G. Bawendi. *Annu. Rev. Mater. Sci.,* 2000, **30**, 545.

6. X. Peng, L. Manna, W. Yang, J. Wickham, E. Scher, A. Kadavanich & A. P. Alivisatos. *Nature,* 2000, **404**, 59 - 61.

7. S. R. Whaley, D. S. English, E. L. Hu, P. F. Barbara & A. M. Belcher. *Nature,* 2000, **405**, 665-668.

8. S.-W. Lee, C. Mao, C. E. Flynn & A. M. Belcher. *Science,* 2002, **296**, 892-895.

9. C. Mao, C. E. Flynn, A. Hayhurst, R. Sweeney, J. Qi, J. Williams, G. Georgiou, B. Iverson & A. M. Belcher. *Proc. Natl. Acad. Sci.,* 2003, **100**, 6946-6941.

10. S.-W. Lee, S.-K. Lee & A. M. Belcher. *Advanced Materials,* 2003, **15**, 689-692.

11. C. E. Flynn, C. Mao, A. Hayhurst, J. L. Williams, G. Georgiou, B. Iverson & A. M. Belcher. *Submitted to Journal of Materials Chemistry,* 2003.

12. C. Y. Yeh, Z. W. Lu, S. Froyen & A. Zunger. *Phys. Rev. B,* 1992, **45**, 12130.

13. Horowize, G. *Adv. Mater.* 1998, 10, 365.

14. Forrest, S.; Burrows, P.; Thomposon, M. *IEEE Spect.* 2000, 37, 29.

15. Schon, J. H.; Meng, H.; Bao, Z. *Nature* 2001, 413, 713.

16. Mirkin, C. A.; Letsinger, R. L.; Mucic, R. C.; Storhoff, J. J. *Nature* 1996, 382, 607.

17. Coffer, J. L.; Bigham, S. R.; Li, X.; Pinizzotto, R. F.; Rho, Y. G.; Pirtle, R. M.; Pirtle, I. L. *Appl. Phys. Lett.* 1996, 69, 3851.

18. Braun, E.; Eichen, Y.; Sivan, U.; Yoseph, G. B. *Nature* 1998, 391, 775.

19. Winfree, B.E.; Liu, F.; Wenzler, L. A.; Seeman, N. C. *Nature* 1998, 394, 539.

20. Mao, C.; Sun, W.; Shen, Z.; Seeman, N. C. *Nature* 1999, 397, 144.

21. Yurke, B.; Turberfield, A. J.; Mills JR, A. P.; Simmel, F.; Neumann, J. L. *Nature* 2000, 406, 605.

22. Whaley, S. R.; English, D.S.; Hu, E. L.; Barbara, P. F.; Belcher, A. M. *Nature* 2000, 405, 665.

23. Aksay, I. A.; Trau, M.; Manne, S.; Honma, I.; Yao, N.; Zhou, L.; Fenter, P.; Eisenberger, P. M.; Gruner, S. M. *Science* 1996, 273, 892.

24. Tanaka, K.; Okahata, Y. *J. Am. Chem. Soc.,* 1996, 118, 10679.

25. Okahata, Y.; Tanaka, K.; *Thin solid Films* 1996, 284-285, 6.

26. Suzuki, H.; Oiwa, K.; Yamada, A.; Sakakibara, H.; Nakayama, H.; Mashiko, S. *Jpn. J. Appl. Phys.* 1995, 34, 3937.

27. Nagayama, K. *Supramolecular Scirnce* 1996, 3, 111.

28. Kay, B. K.; Winter, J.; McCafferty, J. *"Phage Display of Pepitides and Proteins-A Laboratory Manual"*; Academic Press, (1996)

29. Lee, S-W.; Mao, C.; Flynn, C. F.; Belcher, A. M. *Science,* in press.

30. Aharoni, S. M. *Macromolecules* 1979, 12, 94.

31. Aharoni, S. M.; Walsh, E. K. *Macromolecules* 1979, 12, 271.

32. Chen, J. T.; Thomas, E. L.; Ober, C. K.; Hwang, S. S. *Macromolecules* 1995, 28, 1688.

33. Chen, J. T.; Thomas, E. L.; Ober, C. K.; Mao, G. –p. *Science* 1996, 273, 343.

34. Dogic, Z.; Fraden, S. *Langmuir* 2000, 16, 7820.

35. Kralchevsky, P. A.; Paunov, V. N.; Ivanov, I. B.; Nagayama, K. *J. Colloid Interface Sci.* 1992, 151, 79.

36. Denkov, N. D.; Velev, O. D.; Kralchevsky, P. A.; Ivanov, I. B.; Yoshimura, H.; Nagayama, K. *Nature* 1993, 361, 26.

37. Nagayama, K. *Colloids Surfaces A,* 1996, 109, 363.

38. Bowden, N.; Terfort, A.; Carbeck, J.; Whitesides, G. M. *Science* 1997, 276, 233.

39. Tessier, P. M.; Velev, O. D.; Kalambur, A. T.; Lenhoff, A. M.; Rabolt, J. F.; Kaler, E. W. *Adv. Mater.* 2001, 13, 396.

40. Velev, O. D.; Lenhoff, A. M.; Kaler, E. W. *Science* 2000, 287, 2240.

41. Jerome, B. *Rep. Prog. Phys.* 1991, 54, 391.

42. Sonin, A. A.; The Surface Physics of Liquid Crystals, Gordon and Breach, Amsterdam, 1995.

43. Mao, C., Flynn, C.E. and Belcher, A.M. Unpublished data, 2003.

44. Wirde, M.; Gelius, U.; Nyholm, L. *Langmuir* **1999**, 15, 6370.
Wang, J.; Zeng, B.; Fang, C.; Zhou, X. *J. Electroanalyt. Chem.* **2000**, 484, 88.

45. Chen, H. Y.; Zhou, D. M.; Xu, J. J.; Fang, H. Q. *J. Electroanalyt. Chem.* **1997**, 422, 21.
Alexander, P. W.; Rechnite, G. A. *Electroanalysis* **2000**, 12, 343.

46. Harnett, C. K.; Satyalakshmi, K. M.; Craighead, H. G. *Langmuir* **2001**, 17, 178.

47. Sun, X.; He, P.; Liu, S.; Ye, J.; Fang, Y. *Talanta* **1998**, 47, 487.

48. Silin, V.; Weetall, H. *Proc. Annu. Meet. Adhes. Soc. 19th.* **1996**, 211-214.

49. Alivisatos et.al. *Science* 291 **2001**, 2115-2117

50. Reiss et.al. Submitted to *Nature Materials,* 2003.